CHEMISTRY OF MATERIALS

pubs.acs.org/cm

Article

Catalytic Cleavage of the Dative Bond of Ammonia Borane by Polymeric Carbonyl Groups for Enhanced Energy Generation

Prithwish Biswas, Yujie Wang, Steven Herrera, Pankaj Ghildiyal, and Michael R. Zachariah*

Cite This: *Chem. Mater.* 2023, 35, 954−963

Read Online

ACCESS | Metrics & More | Article Recommendations | Supporting Information

ABSTRACT: Dissociation of the dative (B−N) bond of ammonia borane (NH_3BH_3/AB) is essential to prevent its thermochemical oligomerization to chemically resistant BNH_x compounds, for its applicability as a fuel in high-energy propulsion systems. We show that when AB is incorporated into polymer matrices containing carbonyl functional groups, thermal activation causes the carbonyl groups to engage in nucleophilic interactions with AB. Such interactions catalyze the lysis of the dative B−N bond resulting in the decomposition of AB to NH_3 and B_2H_6 gases, with no evidence of oligomerization. We find that the carbonyl groups function as catalysts and do not participate in any net reaction. In situ high-heating rate (~10^5 K/s) characterizations demonstrate that facile-synthesized hierarchical (micro/nano) composite particles of AB/carbonyl-based polymers completely gasify to NH_3 and B_2H_6 at ~510 K, followed by spontaneous ignition in the air with negligible delay. Thus, the current chemical pathway enables the solid-state storage of reactive fuels, NH_3 and B_2H_6, and their controlled on-demand release for high-energy applications.

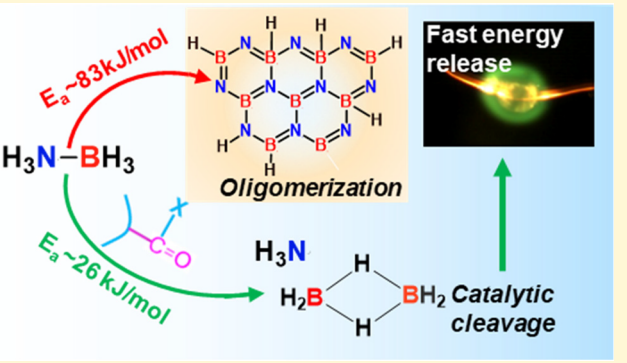

INTRODUCTION

Chemical hydrides such as ammonia borane (AB/NH_3BH_3) have been widely explored as hydrogen storage mediums for low-temperature energy conversion in fuel cells.[1−31] On the other hand, limited efforts have been made[32−35] on investigating the energy generation capability of these compounds for propulsion systems, which demand extremely high-energy release rates.[36−44] Elemental metals and metalloids, particularly boron (B), possess high oxidative energy density and are, therefore, attractive as fuel components in solid-state energy dense materials for propulsion systems.[45] During the oxidation process of B nanoparticles, a molten oxide shell grows from the surface to the core of the particle, while core B is still in the solid state.[46,47] The liquid oxide shell presents a significant barrier to oxygen diffusion, which severely limits the reactivity of particulate B.[48] Borohydride complexes, like AB consisting of both of the highest energy dense elements B (~58 kJ/g) and H (~120 kJ/g), are very attractive as fuels for energetic applications. Additionally, such complexes can potentially decompose to gaseous hydrogen and boranes (BH_x), which in principle can react without condensed phase diffusion limitations.[49−51]

Unfortunately, the dative B−N bond introduces complications to the thermal decomposition mechanism of AB, as it causes AB molecules to oligomerize to higher molecular weight BNH_x compounds, such as gaseous borazine (BZ) and solid-polyborazylene (PBZ), instead of forming ammonia or boranes.[19,32,52−54] Solid-PBZ is often used as a chassis for regenerating AB to facilitate reversible hydrogen storage in AB.[16,19,20] However, in high-energy propulsion systems requiring the oxidation of both B and H elements, these higher molecular weight BNH_x compounds can impede the reactivity and energy generation rate from AB, as chemical resistance increases with molecular weight. Previous studies have employed liquid[34,55−57] and solid-state oxidizers[32] or surrogate exothermic reactions[33] to alter the condensed phase decomposition intermediate of AB, to enhance its energy release rate by inhibiting BNH_x formation. However, this limits the use of AB in propulsion systems using air as an oxidizer.[58,59] Some studies have reported that the interaction with polymer binders can generate NH_3 and H_2 from AB instead of BZ.[60−64] However, those studies are lacking in evidence and discussion on the fate of the boron atoms during AB decomposition.

When neat AB crystals melt, intermolecular hydride transfer between the borons along with subsequent nucleophilic addition of NH_3 moieties to the electrophilic B-center results in the formation of diammoniate of diborane (DADB/

Received: August 31, 2022
Revised: January 18, 2023
Published: January 31, 2023

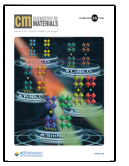

https://doi.org/10.1021/acs.chemmater.2c02684
Chem. Mater. 2023, 35, 954−963

$[NH_3BH_2NH_3]^+[BH_4]^-$) as an intermediate. This activates the oligomerization pathway of AB to BNH_x species.[19,32,52] Herein, we show that the incorporation of AB in matrices of polymers with carbonyl groups, such as polymethyl methacrylate (PMMA), polyvinyl pyrrolidone (PVP), and polypropylene carbonate (PPC), can prevent the oligomerization of AB. The carbonyl groups compete with the borons of AB as sites of nucleophilic attack from the NH_3 moieties, thereby resulting in the catalytic cleavage of the dative B−N bond in AB leading to its dissociation into NH_3 and B_2H_6. Using high-heating rate in situ temperature-jump time-of-flight mass spectrometry (T-jump TOFMS), supported with thermogravimetric analysis and attenuated total reflection/Fourier transform infrared (ATR/FTIR) characterizations, we show that AB completely gasifies to NH_3 and B_2H_6 before the onset of the decomposition of the polymer, which remains chemically intact post-AB decomposition. The measured activation energy of the AB decomposition pathway to NH_3 and B_2H_6 in the polymer matrix (∼26 kJ/mol) is much lower than both the bond-dissociation enthalpy of AB (∼194 kJ/mol) and activation energy of DADB formation (∼83 kJ/mol), confirming the catalytic effects of the polymeric carbonyl groups.

In order to investigate in-operando performance, we adopted a facile and scalable aerosol route for synthesizing 5−10 μm AB/polymer composite particles containing ∼100 nm AB domains. High heating rate measurements revealed that the AB molecules in the composite particles decompose to NH_3 and B_2H_6 at ∼510 K and that the released B_2H_6 spontaneously ignites in the air with negligible ignition delay. B_2H_6 with extremely low auto-ignition temperature ∼ 310 K (H_2 ∼ 850 K) is highly desirable for propulsion systems using air as an oxidizer; however, the use of B_2H_6 in gaseous form has been limited due to its high instability and toxicity.[65,66] The current study solves this issue, by reporting a novel chemical pathway that facilitates the solid-state storage and controlled on-demand release of B_2H_6 for high-energy applications.

EXPERIMENTAL SECTION

Materials. AB (∼97%) powder consisting of ∼50−100 μm crystals was purchased from Sigma Aldrich. Scanning electron microscope (SEM) and X-ray diffraction (XRD) of the as-received AB crystals can be found elsewhere.[32] PMMA (M_W ∼ 550,000), PVP (M_W ∼ 360,000), and PPC (M_W ∼ 283,000) were obtained from Alfa Aesar, Fisher Scientific, and Empower, respectively. All solvents used were obtained from Fisher Scientific.

AB/Polymer Composite Preparation Method for Different Characterizations. For making AB/polymer composites containing different wt % of AB, desired amounts of AB and polymers were completely dissolved in an ethanol−dichloromethane mixture, containing 80% dichloromethane and 20% ethanol by volume, to obtain a completely transparent solution. The polymer-to-solvent ratio is kept constant at 10 mg/mL in all the solutions, and only the AB/polymer ratio has been varied. In the case of the AB/PVP composite, only ethanol was used as the solvent. For the T-jump measurements, the composite solvents were directly drop-casted and dried from the solution as a film on the Pt wire sample holder. The coated samples were allowed to stay under a high vacuum for ∼15 min, before each measurement, to ensure complete removal of the solvents. For other characterizations like thermo-gravimetric analysis (TGA), ATR-FTIR, and XRD, the AB/polymer solutions were dried as solid films on glass petri dishes in a vacuum oven and then transferred to the respective sample holders required for the measurements. The atomic force microscopy (AFM) imaging was performed on AB/PMMA films spin-coated on glass slides using the same formulation.

Characterizations on the Microstructure, Composition, and Thermochemical Reactions of AB/Polymer Composites. ATR-FTIR characterizations have been performed using ThermoFisher Nicolet iS50R, for compositional analysis as well as to characterize the peak splitting due to the dihydrogen bonding of AB. XRD has been performed using PANalytical EMPYREAN (Cu Kα source, λ = 1.54 $\AA$) to identify the composition and degree of crystallinity of AB in polymer matrices. TGA was performed using Netzsch STA 449 F3 to understand the decomposition steps of AB, polymers, and AB/polymer composites at a heating rate of 10 K/min in argon flow. Tapping mode AFM was performed using Asylum Research MFP-3D with a 7 nm Si probe to obtain phase retrace images of the AB domains near the surface of the polymer composites, with the assumption that the microstructure near the surface of the spin-coated thin-films on a glass substrate is identical to that in the bulk. The SEM micrographs of the meso-particle composites were obtained using FEI NNS450.

In Situ Temperature Jump Time-of-Flight Mass Spectrometry and High-Speed Imaging. High heating rates attained during fast exothermic reactions can dramatically influence intrinsic chemical reaction rates and condensed phase diffusivities. Hence, combustion reactions of solid-state fuels need to be probed at high heating rates. Temperature jump probes coupled with a time-of-flight mass spectrometer (T-jump TOFMS) have been used to perform in situ time and temperature-resolved analysis of the gas phase species released on the decomposition of AB, polymers, and AB in polymer matrices at high heating rates of ∼10^5 K/s. Details about the mass spectrometer can be found in several of our previous publications.[32,45,67,68] For the measurements, either AB powder was drop-casted from dispersion in hexane or the dissolved polymer or AB/polymer are drop-casted as films directly from their solutions, on a ∼75 μm Pt wire, which is resistively heated to ∼1500 K with a ∼3 ms voltage pulse, which maintains an average heating rate of ∼10^5 K/s. For the Flynn−Wall−Ozawa activation energy measurements, the heating rate was varied by adjusting the pulse width. The thin coating ensures that the sample is at the same instantaneous temperature of the wire and is uniformly heated. The instantaneous wire temperature is estimated through the Callender−Van-Dusen equation by monitoring the current across the wire at every 0.1 ms over the entire 3 ms pulse. The TOFMS assembly samples the gas phase species released at every 0.1 ms over 10 ms. The entire measurement is performed under a high vacuum of ∼10^{-9} atm. For the high-speed imaging of the ignition process, the same sample holder and heating assembly are used, the only exception being that the heating of the sample is performed in air. A high-speed Phantom Miro 110 camera triggered by the rising edge of the ∼3 ms pulse is used to capture the ignition phenomenon at ∼50,000 frames per second with an exposure of ∼50 μs.

Synthesis of Mesoparticle Composites. The hierarchical micro/nano AB/polymer mesoparticle composites were spray dried using a commercial Büchi B-290 Mini Spray Drier. The precursor solution was made using the same procedure used for making the AB/polymer composite films, except the total AB and polymer content in the solution is reduced to 5 mg/mL. The precursor solution was atomized and dried using heated argon gas at ∼320 K, to make the composite mesoparticles.

RESULTS AND DISCUSSION

High Heating Rate (∼10^5 K/s) Decomposition Products of AB in the PMMA Matrix. High heating rates are required for activating the ignition and combustion process of energetic materials (∼10^5 K/s). Therefore, the decomposition reactions of crystalline AB and AB in the PMMA matrix have been probed in situ by T-jump TOFMS at heating rates of ∼10^5 K/s under a high vacuum (∼10^{-9} atm). As mentioned in the experimental section, a thin layer of sample coated on a ∼75 μm Pt wire is rapidly pulse-heated to ∼1500 K within ∼3

https://doi.org/10.1021/acs.chemmater.2c02684
Chem. Mater. 2023, 35, 954−963

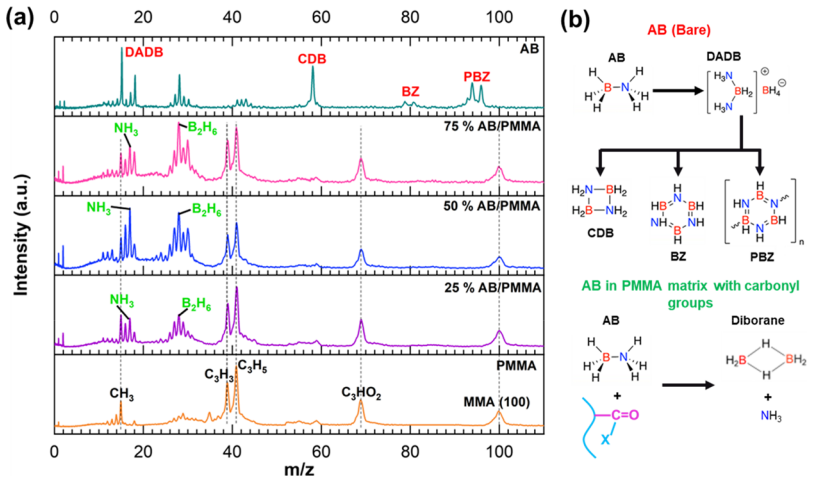

Figure 1. (a) T-jump TOFMS spectra show that bare AB polymerizes to BNH_x species, whereas 25, 50, and 75% by wt. AB in the PMMA matrix decomposes to NH_3 and B_2H_6 when subjected to a temperature ramp (~298−1500 K) within 3 ms at ~10^5 K/s. (b) Schematic explaining the different products formed after decomposition of bare AB and AB in PMMA matrices.

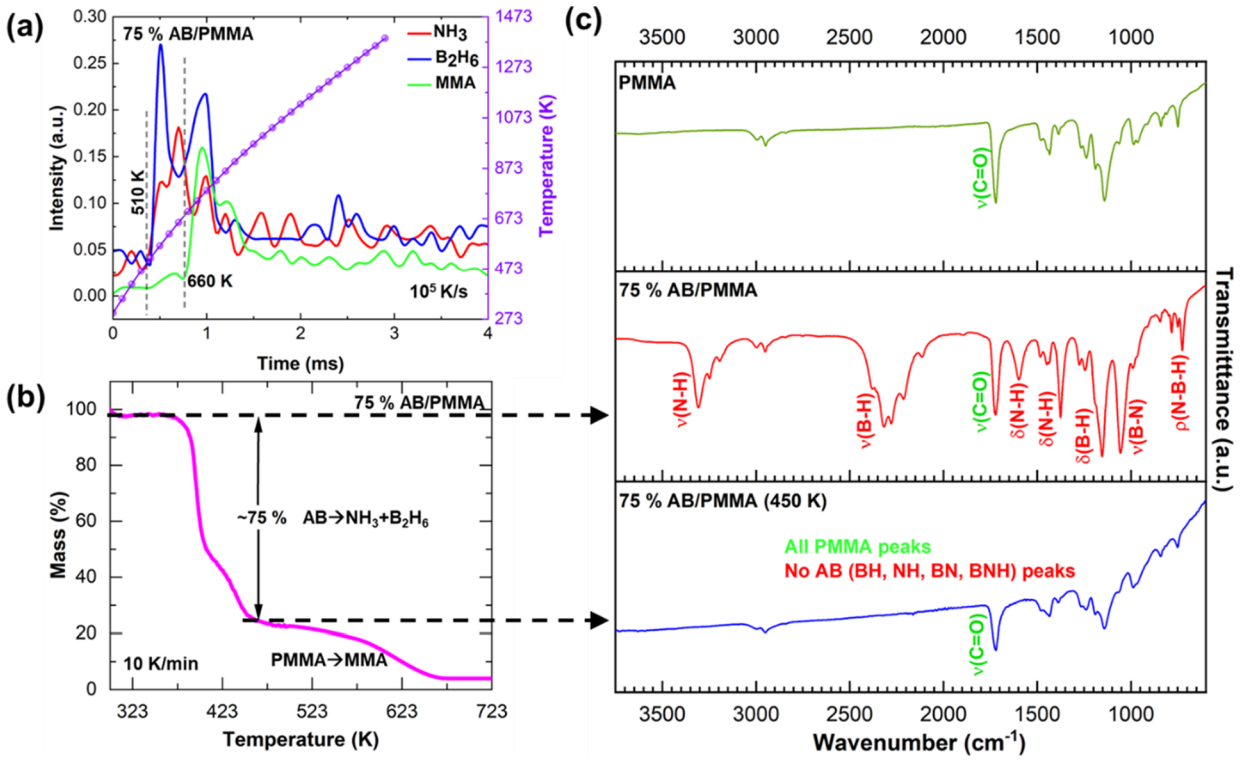

Figure 2. (a) T-jump TOFMS (~10^5 K/s) species release profiles show that AB releases NH_3/B_2H_6 (~510 K) before PMMA unzips to MMA (~660 K). (b) TGA (10 K/min) of 75% AB/PMMA showing that AB completely gasifies to NH_3 and B_2H_6, prior to PMMA decomposition. (c) TGA residue at 450 K shows all the ATR-FTIR signatures of PMMA, indicating that the chemical composition of the polymer is unaltered post-AB decomposition.

ms (T-jump), and the gaseous species evolved on the decomposition of the sample during the temperature ramp is probed over ~10 ms at an interval of 0.1 ms through the TOFMS technique. Figure 1a shows the time-averaged mass spectra of bare AB and 25, 50, and 75 wt % of AB in the PMMA matrix. The composite samples were coated as a film on the Pt wire by drop-casting of respective AB/PMMA precursor solutions.

At these heating rates, crystalline AB powder melts and AB molecules combine in the condensed phase to form DADB, as also reported in previous studies.[19,25,32,52,69] The formation of DADB leads to further oligomerization of DADB and AB molecules into higher molecular weight gas phase BNH_x clusters such as cyclic diborane (CDB) and BZ, simultaneously forming PBZ in the condensed phase (Figure 1b). Signatures of DADB fragments (m/z = 15), CDB (m/z = 58), BZ (m/z = 81), and PBZ fragments (m/z = 94 and 96) are observed in the mass spectra of bare AB shown in Figure 1a. In contrast, BNH_x species are absent in the AB/PMMA composites (Figure 1a). Rather, AB molecules in AB/PMMA generate ammonia (NH_3) and diborane (B_2H_6) (Figure 1b), as evident from the spectra represented in Figure 1a. Thus, AB in the PMMA matrix

https://doi.org/10.1021/acs.chemmater.2c02684
Chem. Mater. 2023, 35, 954−963

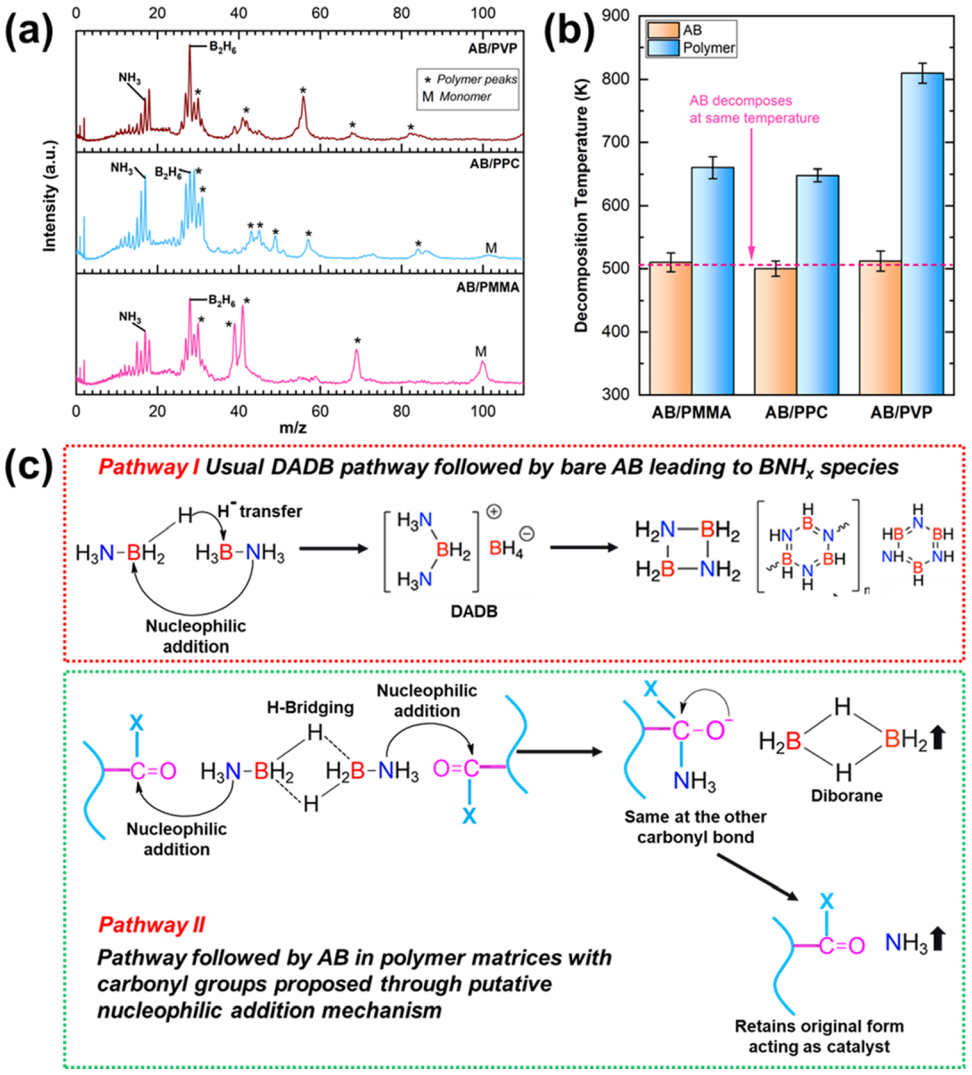

Figure 3. (a) T-jump TOFMS spectra show that AB follows the same pathway releasing NH_3 and B_2H_6 in all polymer matrices with carbonyl groups. (b) Decomposition temperature of AB in all polymer matrices with carbonyl groups is the same (~510 K), irrespective of the polymer decomposition temperature. (c) Differences between the DADB pathway, followed by bare AB, and the NH_3/B_2H_6 pathway, followed by AB in the PMMA matrix, explained based on putative nucleophilic addition reaction and 3-center 2-electron bridge bond formation mechanisms.

follows an alternative decomposition pathway, possibly because of its interaction with the carbonyl groups, the mechanism of which is systematically investigated and revealed in the rest of the article.

Time and Temperature Resolved Decomposition Profiles of AB in the PMMA Matrix. The time-resolved species and temperature evolution profiles (Figure 2a) obtained from T-jump TOFMS measurement of 75% AB/PMMA show that AB decomposes to gaseous NH_3 and B_2H_6 at ~510 K before PMMA unzips to its monomers[70] at ~660 K. The decomposition temperature remains the same for AB/PMMA composites with lower AB content (25 and 50 wt %) as shown in Figure S1 (the supporting information). Generally higher heating rates have higher reaction onset temperatures.[71] At slow heating rates (10 K/min) of TGA in an argon environment, neat PMMA decomposition initiates at ~460 K (Figure S2), whereas neat AB undergoes a two-stage mass loss between ~380 and 480 K, leaving ~40% residue (Figure S3) of PBZ.[32] By contrast, a 75% AB/PMMA composite shows a ~75% mass loss (Figure 2b) between ~360 and 450 K, before the onset of PMMA decomposition. This indicates that AB completely decomposes at ~450 K (slow-heating rate)/~510 K (high-heating rate), to gas phase species before the initiation of PMMA decomposition. The intermediary stage solid residue collected at ~450 K is devoid of all NH, BH, and BN bands of AB and only shows the IR signatures from PMMA (Figure 2c). This also confirms that AB has been completely decomposed to gas phase species prior to PMMA decomposition, without leaving any trace of PBZ. The same observation has been made in TGA (Figure S4) and ATR-FTIR (Figure S5) analysis of 25% AB/PMMA composite. The absence of gas phase PBZ fragments in T-jump TOFMS (Figure 1a) spectra as well as the absence of its IR signatures in the solid-state intermediate residue (Figure 2c) of AB/PMMA composites indicate that PMMA inhibits the polymerization of AB molecules, resulting in its direct decomposition to NH_3 and B_2H_6.

Generic Mechanism of AB Decomposition with All Carbonyl Group Polymers. T-jump TOFMS spectra presented in Figure 3a show that AB (~75% by wt) in matrices of other polymers with carbonyl groups such as PPC and PVP, also decomposes to NH_3 and B_2H_6, rather than polymerizing to BNH_x species. Representative temporal

https://doi.org/10.1021/acs.chemmater.2c02684
Chem. Mater. 2023, 35, 954−963

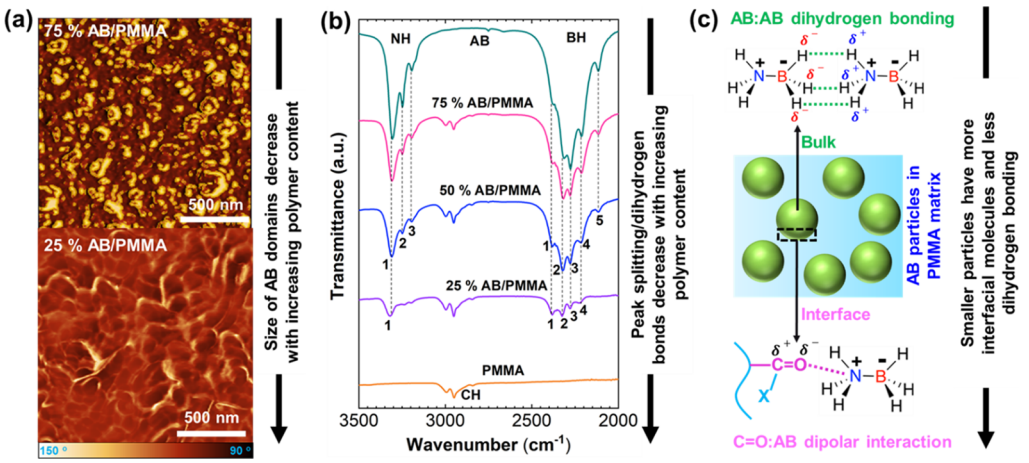

Figure 4. (a) AFM phase-retrace micro-graphs of the 75% AB/PMMA composite shows ∼100 nm AB domains, whereas the AB domains are small and unresolvable in the case of 25% AB/PMMA. (b) Dihydrogen bonding led IR peak splitting of NH and BH bonds decreases with an increase in polymer content. (c) Schematic explaining the dihydrogen bonding between AB molecules at the bulk of the particle phase and the dipolar interaction between AB and polymeric carbonyl groups at the interface.

species and temperature evolution profiles of AB in PPC and PVP matrices are shown in Figures S6 and S7, respectively. Interestingly, AB decomposes at the same temperature of ∼510 K, with all these carbonyl group polymers (PMMA, PVP, and PPC) regardless of the differing decomposition temperatures of the polymers (Figure 3b). Moreover, the decomposition temperature of AB is lower than the polymer decomposition temperature in all these cases. This suggests that the carbonyl groups of the polymers are solely responsible for altering the decomposition pathway of AB. We also show that in non-carbonyl-based polymer matrices such as poly-vinyl alcohol AB follows the usual DADB pathway forming BNH_x species (Figure S8), again proving the necessity of the carbonyl groups for altering the decomposition pathway of AB.

Prior studies have shown that B and H atoms tend to form 3-center 2-electron bridge or banana bonds, due to the electron deficiency of B and the hydridic nature of the H attached to it.[72] Figure 3c shows the interactive behavior of a pair of AB molecules existing in (i) the molten phase of bare AB crystals (Pathway I) and (ii) at the AB/polymer interface when AB is present in the polymer matrix (Pathway II), based on putative nucleophilic addition reaction mechanisms.[73,74] In the first case (Pathway I), intermolecular bridging interactions between the BH_3 groups of two AB molecules facilitate the nucleophilic addition of the NH_3 moiety of the second molecule to the B-center of the first molecule, resulting in a simultaneous hydride ion transfer from the B-center of the first molecule to that of the second molecule, leading to the formation of DADB. This widely accepted pathway has been reported in several previous studies,[19,32,52,69,72] which is also validated by the appearance of DADB and other BNH_x species in the mass spectra of bare AB (Figure 1a). However, at the AB/polymer interface, the proximity between the NH_3 groups of AB and the carbonyl groups of the polymer, results in the nucleophilic addition of the NH_3 groups to the polymeric carbonyl groups (Pathway II), simultaneously leading to a 3-center 2-electron bridge formation between the BH_3 groups. Upon the nucleophilic addition, the oxygen anions will undergo transient bonding with the electron-deficient borons, till the BH_3 groups form the second bridge bond leaving as gaseous diborane (B_2H_6) gas. On the release of B_2H_6, each oxygen anion donates its electron to the carbon to reform the carbonyl bonds, resulting in the release of the attached NH_3. This is also supported by the finding that the carbonyl groups remain intact post-AB decomposition (Figure 2c). Thus, the polymeric carbonyl groups retain their integrity post-AB decomposition, acting as catalysts for the disintegration of the dative B−N bond of AB, thereby generating NH_3 and B_2H_6. This explains the alternative decomposition pathway of the interfacial AB molecules. However, it is still uncertain why the AB molecules at the bulk of the particle phase do not follow the DADB pathway.

Microstructure, Dipolar vs Dihydrogen Bonding: Why the Molecules at the Core of AB Particles Do Not Follow the DADB Pathway. The AB molecule possesses an inherent dipole moment due to its dative B−N bond, with nitrogen and boron as the positive and negative poles, respectively.[18,72] Moreover, the difference in electronegativities causes the H atoms attached to the boron to be hydridic, whereas those attached to the nitrogen are protic. This leads to intermolecular dihydrogen bonding between the AB molecules, which binds them together in the AB crystal.[18,75] While the formation of AB/polymer composites, solvent removal from the AB/polymer solution drives the polymer chains to self-assemble around the nucleating AB particles to form the solid-composite phase. Phase-contrast AFM in tapping mode has been performed on thin AB/PMMA films spin-coated on glass substrates, to image the self-assembled micro-structure of AB/PMMA composites. The AFM measurement can clearly resolve the ∼100 nm AB domains (Figure 4a) embedded near the surface of the 75% AB/PMMA composite film. By contrast, a single uniform polymer phase is observed in the case of 25% AB/PMMA indicating that the AB crystals are much smaller and, hence, the particle phase cannot be resolved. During the self-assembly process, the negative pole (oxygen) of the dipolar carbonyl group[73,74] will have attractive interactions with the acidic protons attached to the nitrogen, and therefore, the polymeric carbonyl group will be in contact with the acidic protons of the interfacial AB molecules after the self-assembly process. Dihydrogen bonding in bare AB splits the IR peaks[63,72] for stretching vibrations of the NH and BH bonds into 3 and 5 peaks, respectively (Figure 4b). The ATR-IR spectra over the entire range of frequencies have been presented in Figure S9. With increasing polymer content, the

https://doi.org/10.1021/acs.chemmater.2c02684
Chem. Mater. 2023, 35, 954−963

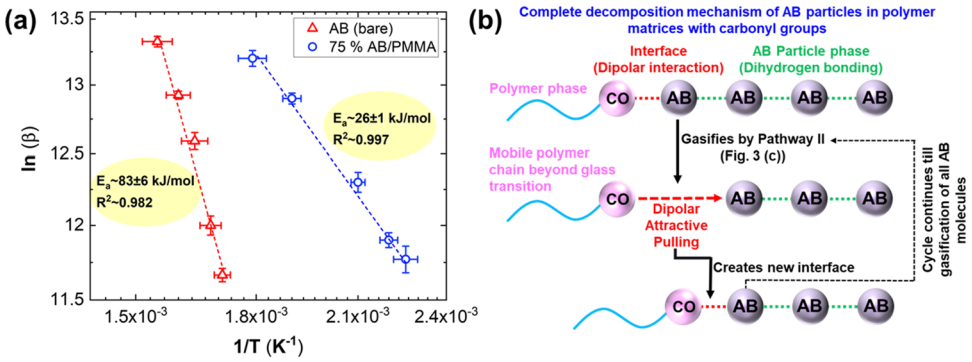

Figure 5. (a) Flynn−Wall−Ozawa activation energy of AB decomposition in the PMMA matrix, obtained from T-jump TOFMS measurements, is ~60 kJ/mol lower than that of the DADB pathway followed by bare AB. (b) Schematic explaining the reason why the AB molecules at the core of the particle phase do not follow the DADB pathway.

peaks merge, as the 25% AB/PMMA only shows 1 peak for the NH band and 4 peaks for the BH band, indicating that the number of dihydrogen bonds decreases with increase in polymer content. Therefore, with an increase in polymer content, the particle size decreases, and the number of interfacial molecules increases, decreasing the number of dihydrogen bonds. This is also confirmed by the sharpening of the XRD peaks of AB with decreasing polymer content in AB/PMMA composites (Figure S10). Although the AB molecules at the particle/polymer interface have dipolar interactions with the carbonyl groups of PMMA, those existing at the bulk of the particle phase are bound by dihydrogen bonding as explained in Figure 4c. In the 25% AB/PMMA composite, AB and MMA are present approximately in a 1:1 molar ratio, which is much lower than the 10:1 AB to MMA molar ratio in the 75% AB/PMMA composite. Thus, the AB in 25% AB/PMMA is expected to be much smaller having much higher interfacial interaction with the carbonyl groups. However, at lower polymer content (~75% AB/PMMA) a significant number of dihydrogen bonded AB molecules exist at the core of the AB particles, which surprisingly do not oligomerize through the DADB pathway. To explain this phenomenon, we measured the activation energies of the DADB pathway and the NH_3/B_2H_6 pathway, to compare their kinetics.

The activation energy barrier of DADB/BNH_x release from bare AB and NH_3/B_2H_6 release from 75% AB/PMMA composite have been determined by the Flynn−Wall−Ozawa method[67] from T-jump TOFMS measurements (Figure 5a). The Flynn−Wall−Ozawa method relates the activation energy (E_a) and heating rate (β) as $\ln(\beta) = -1.05\frac{E_a}{RT} + \text{const.}$, where T is the species release temperature and R is the universal gas constant. The heating pulse width of the T-jump has been adjusted to vary the heating rates and the species (DADB/B_2H_6) release temperatures at various heating rates have been obtained to make the plot in Figure 5a, in order to estimate the activation energies. The B−N bond dissociation enthalpy (BDE) of AB, that is, the enthalpy of the reaction AB → NH_3 + BH_3, is ~177 kJ/mol, as calculated using the standard enthalpies of formation of AB,[76] NH_3 (Active Thermochemical Tables-Argonne National Laboratory), and BH_3.[77] The measured activation energy of bare AB polymerization to BNH_x (Figure 5a) is much lower than the BDE of ~177 kJ/mol. This clearly explains why neat AB oligomerizes on thermal activation, rather than breaking its B−N bond. However, the activation energy of AB decomposition in the PMMA matrix (~26 kJ/mol) is ~60 kJ/mol lower than that of bare AB (~83 kJ/mol), which makes it favored over the DADB pathway.

Additionally, according to Figure 5a, the decomposition temperature of AB in the PMMA matrix is lower than the bare AB decomposition temperature at all heating rates. Given that the decomposition temperature of AB/carbonyl polymer composites is independent of the polymer composition (Figure 3b) and polymer content (Figure S1), it can be assumed that the activation barrier of AB decomposition in all polymer matrices with carbonyl groups will be similar. Based on these facts, an overall decomposition mechanism of the AB particles has been proposed (Figure 5b). During the temperature ramp, the carbonyl groups will initially catalyze the decomposition of interfacial AB molecules (Figure 3c). The interfacial molecules will gasify to NH_3 and B_2H_6, exposing the adjacent underlying layer of AB molecules. As this process is initiated (Figure 3b) beyond the glass transition temperatures of PMMA/PPC/PVP, the freshly exposed AB layer will attract the mobile polymer chains through dipolar interactions, which can move and fill the angstrom scale gap, creating a new particle/polymer interface. The interfacial AB molecules will decompose again exposing the underlying AB molecular layer, which will form a new interface with the polymer. This cycle will continue till all the underlying subsequent layers of AB molecules are gasified to NH_3 and B_2H_6 in a shrinking-core fashion. Since this entire process happens at a lower temperature and at a faster rate (~60 kJ/mol lower E_a) than the DADB pathway, AB particles in a polymer matrix containing carbonyl groups will be completely decomposed before the activation of the DADB pathway. Moreover, as the polymers decompose at higher temperatures, the polymers and the carbonyl groups will remain intact till the entire consumption of the AB particles, thereby acting as catalysts for AB decomposition. This explains why the AB molecules at the core of the particle phase do not follow the DADB pathway.

AB/PMMA Composites with Mesoscopic Architectures. The characterizations described so far are performed on AB/polymer composite films formed by evaporation of the solvents from their respective solutions. For practical viability, there is considerable interest in hierarchical assembly of nanoparticles into mesoscale architectures due to ease of processing.[78−81] Hence, for in-operando characterizations we have adopted an aerosol-based approach, to atomize a solution of 75% AB/PMMA, and dry it on the fly with heated argon at ~320 K (Figure 6a), in order to make ~5−10 μm mesoscale composite particles of AB/PMMA, as represented through the

https://doi.org/10.1021/acs.chemmater.2c02684
Chem. Mater. 2023, 35, 954−963

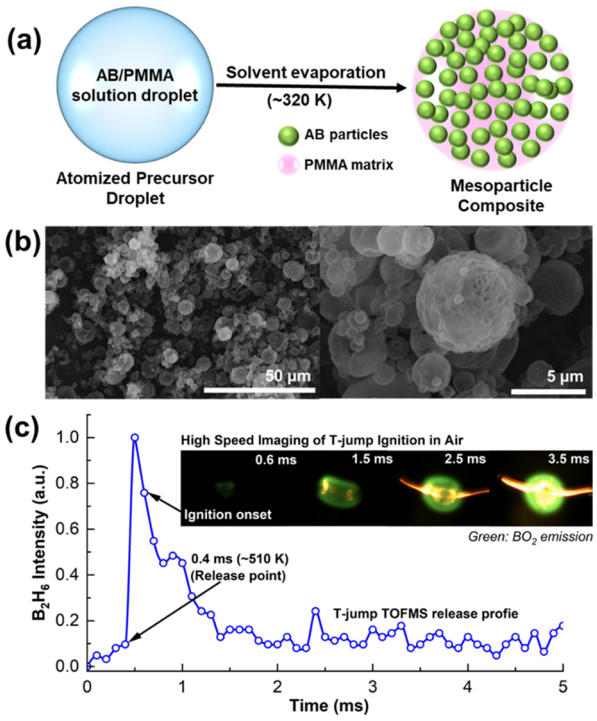

Figure 6. (a) Schematic describing the aerosol route for synthesis of mesoscale hierarchical AB/PMMA composite particles. (b) SEM micrographs of the synthesized mesoparticles. (c) T-jump TOFMS B_2H_6 release profile and snapshots of the ignition process of the AB/PMMA mesoparticle composite in the air.

SEM micrographs in Figure 6b. As 75 wt % of AB results in ~100 nm AB domains in AB/PMMA composites (Figure 4a), the spray-dried 75% AB/PMMA composite particles will likely be a hierarchical assembly of nanoscale AB domains. T-jump TOFMS spectra of the 75% AB/PMMA composite mesoparticles (Figure S11) match with that of the 75% AB/PMMA composite film (Figure 1a) and the B_2H_6 release temperature of the mesoparticles remains the same at ~510 K (Figure 6c). This indicates that the mesoparticles follow the same chemical decomposition pathway described in the previous sections. The inset of Figure 6c shows that the first instance of the green BO_2 emission (~0.6 ms) designated as the ignition onset is observed ~0.2 ms after the initiation of B_2H_6 release (~0.4 ms). The negligible ignition delay (~0.2 ms) indicates that B_2H_6 spontaneously ignites in the air on its release, which is expected from its low autoignition temperature (~310 K).[65]

Therefore, AB/PMMA composite particles can be used for the generation of reactive gases such as NH_3 and B_2H_6. Polymers with carbonyl groups such as PMMA can be used both as a hydrophobic (~protection from moisture) binding agent as well as a chemical component for altering the decomposition pathway of AB generating lower molecular weight reactive species. The low auto-ignition temperature or high reactivity of B_2H_6 (~310 K) compared to both H_2 (~850 K) and NH_3 (~1000 K)[65,82,83] makes it extremely desirable for processes requiring rapid energy release. As B_2H_6 gas is extremely unstable and toxic, storing and using it in gaseous form is difficult.[66] However, AB/PMMA composites can serve as solid-state B_2H_6 storage materials, which when thermally activated can release B_2H_6, hence producing energy on-demand. As the polymer stays intact post-AB decomposition, technologies can be designed to separate the combustion zone of released NH_3 and B_2H_6 from the surface of the polymer, so that the polymer can be recycled. Hence, these fundamental findings will open up multiple possibilities of applied research on making sustainable materials for energy storage.

CONCLUSIONS

In this study, we have shown that on thermal activation polymeric carbonyl groups catalyze the dissociation of the dative B−N bond of AB through nucleophilic interactions, by generating reactive NH_3 and B_2H_6 gases. This prevents AB to oligomerize to chemically resistant higher molecular weight BNH_x species. The carbonyl groups lower the activation energy of B−N bond dissociation to ~26 kJ/mol, which is much lower than the BDE (~194 kJ/mol) as well as the activation energy (~83 kJ/mol) of the BNH_x pathway, thereby resulting in the catalytic cleavage of the B−N bond. We have also shown that a facile and scalable aerosol spray drying approach can be employed to synthesize hierarchical (micro/nano) AB/polymer composite particles with AB as the major component (~75 wt %). Through in situ high heating rate characterizations, we have shown that the composite particles release NH_3 and B_2H_6 on thermal activation at ~510 K, and the released B_2H_6 spontaneously ignites in the air with negligible delay. The generation of lower molecular weight reactive species instead of chemically resistant BNH_x species through this pathway makes AB suitable as a fuel for high-energy applications.

ASSOCIATED CONTENT

Supporting Information

The Supporting Information is available free of charge at https://pubs.acs.org/doi/10.1021/acs.chemmater.2c02684.

Additional supporting data from TGA, mass spectrometry, and IR spectroscopies for different polymer content and composition (PDF)

AUTHOR INFORMATION

Corresponding Author

Michael R. Zachariah − *University of California, Riverside, California 92521, United States;* orcid.org/0000-0002-4115-3324; Email: mrz@engr.ucr.edu

Authors

Prithwish Biswas − *University of California, Riverside, California 92521, United States;* orcid.org/0000-0002-9921-2905

Yujie Wang − *University of California, Riverside, California 92521, United States*

Steven Herrera − *University of California, Riverside, California 92521, United States*

Pankaj Ghildiyal − *University of California, Riverside, California 92521, United States; University of Maryland, College Park, Maryland 20742, United States;* orcid.org/0000-0002-4422-3068

Complete contact information is available at: https://pubs.acs.org/10.1021/acs.chemmater.2c02684

Notes

The authors declare no competing financial interest.

https://doi.org/10.1021/acs.chemmater.2c02684
Chem. Mater. 2023, 35, 954−963

■ ACKNOWLEDGMENTS

We gratefully acknowledge support from the ONR and the DTRA-URA on Materials Science in Extreme Environments (HDTRA1-20-2-0001). We are also thankful to the CFAMM at the University of California, Riverside, for supporting microscopy instrumentation. We also thank the Winston Chung Global Energy Center and Dr. Reza Abbaschian for assistance with AFM.

■ REFERENCES

(1) Schlapbach, L.; Züttel, A. Hydrogen Storage Materials for Mobile Applications. *Nature* **2001**, *414*, 353−358.
(2) Ngene, P.; Longo, A.; Mooij, L.; Bras, W.; Dam, B. Metal-Hydrogen Systems with an Exceptionally Large and Tunable Thermodynamic Destabilization. *Nat. Commun.* **2017**, *8*, 1846.
(3) Cao, H.; Georgopanos, P.; Capurso, G.; Pistidda, C.; Weigelt, F.; Chaudhary, A. L.; Filiz, V.; Tseng, J. C.; Wharmby, M. T.; Dornheim, M.; Abetz, V.; Klassen, T. Air-Stable Metal Hydride-Polymer Composites of $Mg(NH_2)_2$−LiH and TPX. *Mater. Today Energy* **2018**, *10*, 98−107.
(4) Schneemann, A.; White, J. L.; Kang, S.; Jeong, S.; Wan, L. F.; Cho, E. S.; Heo, T. W.; Prendergast, D.; Urban, J. J.; Wood, B. C.; Allendorf, M. D.; Stavila, V. Nanostructured Metal Hydrides for Hydrogen Storage. *Chem. Rev.* **2018**, *118*, 10775−10839.
(5) Ambrosi, A.; Chua, C. K.; Bonanni, A.; Pumera, M. Lithium Aluminum Hydride as Reducing Agent for Chemically Reduced Graphene Oxides. *Chem. Mater.* **2012**, *24*, 2292−2298.
(6) Zhang, J.; Zhu, Y.; Lin, H.; Liu, Y.; Zhang, Y.; Li, S.; Ma, Z.; Li, L. Metal Hydride Nanoparticles with Ultrahigh Structural Stability and Hydrogen Storage Activity Derived from Microencapsulated Nanoconfinement. *Adv. Mater.* **2017**, *29*, No. 1700760.
(7) Kim, G. J.; Hwang, H. T. Thermal Hydrolysis of Solid-State Sodium Borohydride for Noncatalytic Hydrogen Generation. *Chem. Eng. J.* **2021**, *424*, No. 130445.
(8) Demirci, U. B.; Miele, P. Sodium Borohydride versus Ammonia Borane, in Hydrogen Storage and Direct Fuel Cell Applications. *Energy Environ. Sci.* **2009**, *2*, 627−637.
(9) Concha, B. M.; Chatenet, M.; Maillard, F.; Ticianelli, E. A.; Lima, F. H. B.; de Lima, R. B. In Situ Infrared (FTIR) Study of the Mechanism of the Borohydride Oxidation Reaction. *Phys. Chem. Chem. Phys.* **2010**, *12*, 11507−11516.
(10) Rostamikia, G.; Janik, M. J. Direct Borohydride Oxidation: Mechanism Determination and Design of Alloy Catalysts Guided by Density Functional Theory. *Energy Environ. Sci.* **2010**, *3*, 1262−1274.
(11) Staubitz, A.; Robertson, A. P. M.; Manners, I. Ammonia-Borane and Related Compounds as Dihydrogen Sources. *Chem. Rev.* **2010**, *110*, 4079−4124.
(12) Simagina, V. I.; Vernikovskaya, N. V.; Komova, O. V.; Kayl, N. L.; Netskina, O. V.; Odegova, G. V. Experimental and Modeling Study of Ammonia Borane-Based Hydrogen Storage Systems. *Chem. Eng. J.* **2017**, *329*, 156−164.
(13) Stephens, F. H.; Baker, R. T.; Matus, M. H.; Grant, D. J.; Dixon, D. A. Acid Initiation of Ammonia-Borane Dehydrogenation for Hydrogen Storage. *Angew. Chem., Int. Ed.* **2007**, *46*, 746−749.
(14) Wang, F.; Planas, O.; Cornella, J. Bi(I)-Catalyzed Transfer-Hydrogenation with Ammonia-Borane. *J. Am. Chem. Soc.* **2019**, *141*, 4235−4240.
(15) Wang, C.; Tuninetti, J.; Wang, Z.; Zhang, C.; Ciganda, R.; Salmon, L.; Moya, S.; Ruiz, J.; Astruc, D. Hydrolysis of Ammonia-Borane over Ni/ZIF-8 Nanocatalyst: High Efficiency, Mechanism, and Controlled Hydrogen Release. *J. Am. Chem. Soc.* **2017**, *139*, 11610−11615.
(16) Demirci, U. B. Ammonia Borane: An Extensively Studied, Though Not yet Implemented, Hydrogen Carrier. *Energies* **2020**, *13*, 3071.
(17) Bhunya, S.; Zimmerman, P. M.; Paul, A. Unraveling the Crucial Role of Metal-Free Catalysis in Borazine and Polyborazylene Formation in Transition-Metal-Catalyzed Ammonia-Borane Dehydrogenation. *ACS Catal.* **2015**, *5*, 3478−3493.
(18) Rizzi, V.; Polino, D.; Sicilia, E.; Russo, N.; Parrinello, M. The Onset of Dehydrogenation in Solid Ammonia Borane: An Ab Initio Metadynamics Study. *Angew. Chem., Int. Ed.* **2019**, *131*, 4016−4020.
(19) Demirci, U. B. Mechanistic Insights into the Thermal Decomposition of Ammonia Borane, a Material Studied for Chemical Hydrogen Storage. *Inorg. Chem. Front.* **2021**, *8*, 1900−1930.
(20) Valero-Pedraza, M. J.; Cot, D.; Petit, E.; Aguey-Zinsou, K. F.; Alauzun, J. G.; Demirci, U. B. Ammonia Borane Nanospheres for Hydrogen Storage. *ACS Appl. Nano Mater.* **2019**, *2*, 1129−1138.
(21) Weismiller, M. R.; Wang, S. Q.; Chowdhury, A.; Thynell, S. T.; Yetter, R. A. Confined Rapid Thermolysis Studies of Ammonia Borane. *Thermochim. Acta* **2013**, *551*, 110−117.
(22) Himmelberger, D. W.; Alden, L. R.; Bluhm, M. E.; Sneddon, L. G. Ammonia Borane Hydrogen Release in Ionic Liquids. *Inorg. Chem.* **2009**, *48*, 9883−9889.
(23) Yang, J. B.; Lamsal, J.; Cai, Q.; James, W. J.; Yelon, W. B. Structural Evolution of Ammonia Borane for Hydrogen Storage. *Appl. Phys. Lett.* **2008**, *92*, No. 091916.
(24) Wahab, M. A.; Zhao, H.; Yao, X. D. Nano-Confined Ammonia Borane for Chemical Hydrogen Storage. *Front. Chem. Sci. Eng.* **2012**, *6*, 27−33.
(25) Gutowska, A.; Li, L.; Shin, Y.; Wang, C. M.; Li, X. S.; Linehan, J. C.; Smith, R. S.; Kay, B. D.; Schmid, B.; Shaw, W.; Gutowski, M.; Autrey, T. Nanoscaffold Mediates Hydrogen Release and the Reactivity of Ammonia Borane. *Angew. Chem., Int. Ed.* **2005**, *117*, 3644−3648.
(26) Yao, Y.; Yong, X.; Tse, J. S.; Greschner, M. J. Dihydrogen Bonding in Compressed Ammonia Borane and Its Roles in Structural Stability. *J. Phys. Chem. C* **2014**, *118*, 29591−29598.
(27) Petit, J. F.; Demirci, U. B. Discrepancy in the Thermal Decomposition/Dehydrogenation of Ammonia Borane Screened by Thermogravimetric Analysis. *Int. J. Hydrogen Energy* **2019**, *44*, 14201−14206.
(28) Chatterjee, T.; Thynell, S. T. Development of a Reaction Mechanism for Liquid-Phase Decomposition of Ammonia Borane. *Thermochim. Acta* **2019**, *682*, No. 178427.
(29) Kumar, V.; Roy, B.; Sharma, P. Kinetics of Borazine Formation from Ammonia Borane Dehydrocoupling Reaction through Ab Initio Analysis. *Int. J. Hydrogen Energy* **2019**, *44*, 22022−22031.
(30) Yang, Z.; Zhou, D.; Chen, B.; Liu, Z.; Xia, Q.; Zhu, Y.; Xia, Y. Improved Hydrogen Release from Ammonia Borane Confined in Microporous Carbon with Narrow Pore Size Distribution. *J. Mater. Chem. A* **2017**, *5*, 15395−15400.
(31) Umemoto, H.; Miyata, A. Decomposition Processes of Diborane and Borazane (Ammonia-Borane Complex) on Hot Wire Surfaces. *Thin Solid Films* **2015**, *595*, 231−234.
(32) Biswas, P.; Ghildiyal, P.; Kwon, H.; Wang, H.; Alibay, Z.; Xu, F.; Wang, Y.; Wong, B. M.; Zachariah, M. R. Rerouting Pathways of Solid-State Ammonia Borane Energy Release. *J. Phys. Chem. C* **2021**, *126*, 48−57.
(33) Rodriguez, D. A.; Dreizin, E. L.; Shafirovich, E. Hydrogen Generation from Ammonia Borane and Water through Combustion Reactions with Mechanically Alloyed Al·Mg Powder. *Combust. Flame* **2015**, *162*, 1498−1506.
(34) Baier, M. J.; McDonald, A. J.; Clements, K. A.; Goldenstein, C. S.; Son, S. F. High-Speed Multi-Spectral Imaging of the Hypergolic Ignition of Ammonia Borane. *Proc. Combust. Inst.* **2021**, *38*, 4433−4440.
(35) Weismiller, M. R.; Duin, A. C. T. V.; Lee, J.; Yetter, R. A. ReaxFF Reactive Force Field Development and Applications for Molecular Dynamics Simulations of Ammonia Borane Dehydrogenation and Combustion. *J. Phys. Chem. A* **2010**, *114*, 5485−5492.
(36) Biswas, P.; Xu, F.; Ghildiyal, P.; Zachariah, M. R. In-Situ Thermochemical Shock-Induced Stress at the Metal/Oxide Interface Enhances Reactivity of Aluminum Nanoparticles. *ACS Appl. Mater. Interfaces* **2022**, *14*, 26782−26790.

(37) Connell, T. L.; Risha, G. A.; Yetter, R. A.; Young, G.; Sundaram, D. S.; Yang, V. Combustion of Alane and Aluminum with Water for Hydrogen and Thermal Energy Generation. *Proc. Combust. Inst.* **2011**, *33*, 1957−1965.
(38) Kline, D. J.; Rehwoldt, M. C.; Wang, H.; Eckman, N. E.; Zachariah, M. R. Why Does Adding a Poor Thermal Conductor Increase Propagation Rate in Solid Propellants? *Appl. Phys. Lett.* **2019**, *115*, No. 114101.
(39) McClain, M. S.; Gunduz, I. E.; Son, S. F. Additive Manufacturing of Ammonium Perchlorate Composite Propellant with High Solids Loadings. *Proc. Combust. Inst.* **2019**, *37*, 3135−3142.
(40) Wang, H.; Kline, D. J.; Zachariah, M. R. In-Operando High-Speed Microscopy and Thermometry of Reaction Propagation and Sintering in a Nanocomposite. *Nat. Commun.* **2019**, *10*, 3032.
(41) Ma, X.; Li, Y.; Hussain, I.; Shen, R.; Yang, G.; Zhang, K.; Ma, X.; Li, Y.; Hussain, I.; Zhang, K.; Shen, R.; Yang, G. Core−Shell Structured Nanoenergetic Materials: Preparation and Fundamental Properties. *Adv. Mater.* **2020**, *32*, No. 2001291.
(42) Jiang, Y.; Deng, S.; Hong, S.; Zhao, J.; Huang, S.; Wu, C. C.; Gottfried, J. L.; Nomura, K. I.; Li, Y.; Tiwari, S.; Kalia, R. K.; Vashishta, P.; Nakano, A.; Zheng, X. Energetic Performance of Optically Activated Aluminum/Graphene Oxide Composites. *ACS Nano* **2018**, *12*, 11366−11375.
(43) Jiang, Y.; Deng, S.; Hong, S.; Tiwari, S.; Chen, H.; Nomura, K. I.; Kalia, R. K.; Nakano, A.; Vashishta, P.; Zachariah, M. R.; Zheng, X. Synergistically Chemical and Thermal Coupling between Graphene Oxide and Graphene Fluoride for Enhancing Aluminum Combustion. *ACS Appl. Mater. Interfaces* **2020**, *12*, 7451−7458.
(44) Zhang, Q.; Shreeve, J. M. Energetic Ionic Liquids as Explosives and Propellant Fuels: A New Journey of Ionic Liquid Chemistry. *Chem. Rev.* **2014**, *114*, 10527−10574.
(45) Wang, Y.; Wang, H.; Xu, F.; Ghildiyal, P.; Zachariah, M. R. Effect of Alkali Metal Perchlorate and Iodate Type on Boron Ignition: The Role of Oxidizer Phase Change. *Chem. Eng. J.* **2022**, *446*, No. 136786.
(46) Chintersingh, K. L.; Schoenitz, M.; Dreizin, E. L. Boron Doped with Iron: Preparation and Combustion in Air. *Combust. Flame* **2019**, *200*, 286−295.
(47) Mursalat, M.; Schoenitz, M.; Dreizin, E. L. Effect of Particle Morphology on Reactivity, Ignition and Combustion of Boron Powders. *Fuel* **2022**, *324*, No. 124538.
(48) Veith, J.; Pfitzner, M. Combustion of Boron Particles in Premixed Methane/Air Flames. *Propell. Explos. Pyrot.* **2016**, *41*, 260−266.
(49) Jeon, E.; Cho, Y. W. Mechanochemical Synthesis and Thermal Decomposition of Zinc Borohydride. *J. Alloys Compd.* **2006**, *422*, 273−275.
(50) Mazaheri, A.; Javadi, M.; Abdi, Y. Chemical Vapor Deposition of Two-Dimensional Boron Sheets by Thermal Decomposition of Diborane. *ACS Appl. Mater. Interfaces* **2021**, *13*, 8844−8850.
(51) Kanth, J. V. B.; Brown, H. C. Improved Procedures for the Generation of Diborane from Sodium Borohydride and Boron Trifluoride. *Inorg. Chem.* **2000**, *39*, 1795−1802.
(52) Stowe, A. C.; Shaw, W. J.; Linehan, J. C.; Schmid, B.; Autrey, T. In Situ Solid State 11B MAS-NMR Studies of the Thermal Decomposition of Ammonia Borane: Mechanistic Studies of the Hydrogen Release Pathways from a Solid State Hydrogen Storage Material. *Phys. Chem. Chem. Phys.* **2007**, *9*, 1831−1836.
(53) Nguyen, V. S.; Matus, M. H.; Nguyen, M. T.; Dixon, D. A. Reactions of Diborane with Ammonia and Ammonia Borane: Catalytic Effects for Multiple Pathways for Hydrogen Release. *J. Phys. Chem. A* **2008**, *112*, 9946−9954.
(54) Nguyen, M. T.; Nguyen, V. S.; Matus, M. H.; Gopakumar, G.; Dixon, D. A. Molecular Mechanism for H_2 Release from BH_3NH_3, Including the Catalytic Role of the Lewis Acid BH3. *J. Phys. Chem . A* **2007**, *111*, 679−690.
(55) Baier, M. J.; Ramachandran, P. V.; Son, S. F. Characterization of the Hypergolic Ignition Delay of Ammonia Borane. *J. Propul. Power* **2019**, *35*, 182−189.
(56) Clements, K. A.; Baier, M. J.; Veeraraghavan Ramachandran, P.; Son, S. F. Experimental Study of Factors Affecting Hypergolic Ignition of Ammonia Borane. *J. Propul. Power* **2021**, *37*, 202−210.
(57) Pfeil, M. A.; Groven, L. J.; Lucht, R. P.; Son, S. F. Effects of Ammonia Borane on the Combustion of an Ethanol Droplet at Atmospheric Pressure. *Combust. Flame* **2013**, *160*, 2194−2203.
(58) Gobin, B.; Harvey, N.; Young, G. Combustion Characteristics of Electrically Controlled Solid Propellants Using Polymer Electrolytes. *Combust. Flame* **2022**, *244*, No. 112291.
(59) Marchioni, F.; Cappelli, M. A. Extended Channel Hall Thruster for Air-Breathing Electric Propulsion. *J. Appl. Phys.* **2021**, *130*, No. 053306.
(60) Seemaladinne, R.; Pati, S.; Kharel, K.; Bafana, A.; al-Wahish, A.; Wujcik, E. K.; Günaydın-Şen, Ö. Ammonia Borane with Polyvinylpyrrolidone as a Hydrogen Storage Material: Comparison of Different Molecular Weights. *J. Phys. Chem. Solids* **2017**, *110*, 394−400.
(61) Zhao, J.; Shi, J.; Zhang, X.; Cheng, F.; Liang, J.; Tao, Z.; Chen, J. A Soft Hydrogen Storage Material: Poly(Methyl Acrylate)-Confined Ammonia Borane with Controllable Dehydrogenation. *Adv. Mater.* **2010**, *22*, 394−397.
(62) Kharel, K.; Gangineni, R.; Günaydın-Şen, Ö. Low Temperature Phase Transition Studies of Ammonia Borane-Polyacrylamide Composites. *Mater. Chem. Phys.* **2018**, *216*, 354−364.
(63) Ploszajski, A. R.; Billing, M.; Nathanson, A. S.; Vickers, M.; Bennington, S. M. Freeze-Dried Ammonia Borane-Polyethylene Oxide Composites: Phase Behaviour and Hydrogen Release. *Int. J. Hydrogen Energy* **2018**, *43*, 5645−5656.
(64) Li, S. F.; Tang, Z. W.; Tan, Y. B.; Yu, X. B. Polyacrylamide Blending with Ammonia Borane: A Polymer Supported Hydrogen Storage Composite. *J. Phys. Chem. C* **2012**, *116*, 1544−1549.
(65) Savel'ev, A. M.; Kuleshov, P. S.; Lukhovitskii, B. I.; Pelevkin, A. V.; Savel'eva, V. A.; Sharipov, A. S. On the Kinetic Mechanism of Ignition of Diborane Mixtures with Air. *Combust. Explos. Shock Waves* **2020**, *56*, 249−266.
(66) Jones, N. B.; Gibbons, B.; Morris, A. J.; Morris, J. R.; Troya, D. Reversible Dissociation for Effective Storage of Diborane Gas within the UiO-66-NH_2Metal-Organic Framework. *ACS Appl. Mater. Interfaces* **2022**, *14*, 8322−8332.
(67) Jian, G.; Zhou, L.; Piekiel, N. W.; Zachariah, M. R. Low Effective Activation Energies for Oxygen Release from Metal Oxides: Evidence for Mass-Transfer Limits at High Heating Rates. *ChemPhysChem* **2014**, *15*, 1666−1672.
(68) Rehwoldt, M. C.; Wang, Y.; Xu, F.; Ghildiyal, P.; Zachariah, M. R. High-Temperature Interactions of Metal Oxides and a PVDF Binder. *ACS Appl. Mater. Interfaces* **2022**, *14*, 8938−8946.
(69) Heldebrant, D. J.; Karkamkar, A.; Hess, N. J.; Bowden, M.; Rassat, S.; Feng, Z.; Rappe, K.; Autrey, T. The Effects of Chemical Additives on the Induction Phase in Solid-State Thermal Decomposition of Ammonia Borane. *Chem. Mater.* **2008**, *20*, 5332−5336.
(70) Blanchet, G. B.; Fincher, C. R. Laser Induced Unzipping: A Thermal Route to Polymer Ablation. *Appl. Phys. Lett.* **1998**, *65*, 1311.
(71) Xu, F.; Nava, G.; Biswas, P.; Dulalia, I.; Wang, H.; Alibay, Z.; Gale, M.; Kline, D. J.; Wagner, B.; Mangolini, L.; Zachariah, M. R. Energetic Characteristics of Hydrogenated Amorphous Silicon Nanoparticles. *Chem. Eng. J.* **2022**, *430*, No. 133140.
(72) Lipscomb, W. N.*Boron Hydrides*; Dover Publications, 2013.
(73) Kamer, K. J.; Choudhary, A.; Raines, R. T. Intimate Interactions with Carbonyl Groups: Dipole-Dipole or n $\rightarrow\pi^*$? *J. Org. Chem.* **2013**, *78*, 2099−2103.
(74) Newberry, R. W.; Raines, R. T. The $\vec{N}\pi*$ Interaction. *Acc. Chem. Res.* **2017**, *50*, 1838−1846.
(75) Klooster, W. T.; Koetzle, T. F.; Siegbahn, P. E. M.; Richardson, T. B.; Crabtree, R. H. Study of the N-H···H-B Dihydrogen Bond Including the Crystal Structure of BH3NH3 by Neutron Diffraction. *J. Am. Chem. Soc.* **1999**, *121*, 6337−6343.
(76) Kondrat'Ev, Y. V.; Butlak, A. V.; Kazakov, I. V.; Timoshkin, A. Y. Sublimation and Thermal Decomposition of Ammonia Borane:

Competitive Processes Controlled by Pressure. *Thermochim. Acta* **2015**, *622*, 64−71.
(77) Yu, C. L.; Bauer, S. H. Thermochemistry of the Boranes. *J. Phys. Chem. Ref. Data* **1998**, *27*, 807.
(78) Yao, H.-B.; Fang, H. Y.; Wang, X. H.; Yu, S. H. Hierarchical Assembly of Micro-/Nano-Building Blocks: Bio-Inspired Rigid Structural Functional Materials. *Chem. Soc. Rev.* **2011**, *40*, 3764−3785.
(79) Qiu, W.; Li, G.; Luo, D.; Zhang, Y.; Zhao, Y.; Zhou, G.; Shui, L.; Wang, X.; Chen, Z. Hierarchical Micro-Nanoclusters of Bimetallic Layered Hydroxide Polyhedrons as Advanced Sulfur Reservoir for High-Performance Lithium−Sulfur Batteries. *Adv. Sci.* **2021**, *8*, No. 2003400.
(80) Lu, Y.; Fan, H.; Stump, A.; Ward, T. L.; Rieker, T.; Brinker, C. J. Aerosol-Assisted Self-Assembly of Mesostructured Spherical Nanoparticles. *Nature* **1999**, *398*, 223−226.
(81) Jia, X.; Chen, Z.; Cui, X.; Peng, Y.; Wang, X.; Wang, G.; Wei, F.; Lu, Y. Building Robust Architectures of Carbon and Metal Oxide Nanocrystals toward High-Performance Anodes for Lithium-Ion Batteries. *ACS Nano* **2012**, *6*, 9911−9919.
(82) He, X.; Shu, B.; Nascimento, D.; Moshammer, K.; Costa, M.; Fernandes, R. X. Auto-Ignition Kinetics of Ammonia and Ammonia/Hydrogen Mixtures at Intermediate Temperatures and High Pressures. *Combust. Flame* **2019**, *206*, 189−200.
(83) Chen, J.; Jiang, X.; Qin, X.; Huang, Z. Effect of Hydrogen Blending on the High Temperature Auto-Ignition of Ammonia at Elevated Pressure. *Fuel* **2021**, *287*, No. 119563.

https://doi.org/10.1021/acs.chemmater.2c02684
Chem. Mater. 2023, 35, 954−963